Appl. Phys. B (2015) 118:439–447
DOI 10.1007/s00340-015-6007-2

Applied Physics B
Lasers and Optics

Broadband and wide-angle antireflective characteristics of nanoporous anodic alumina films for silicon-based optoelectronic applications

Bhaskar Dudem · Jung Woo Leem · Minkyu Choi · Jae Su Yu

Received: 21 August 2014 / Accepted: 6 January 2015 / Published online: 20 January 2015
© Springer-Verlag Berlin Heidelberg 2015

Abstract Nanoporous anodic alumina (NPAA) films are fabricated on silicon (Si) surfaces by the anodization of aluminum (Al). Effect of the thickness of initial Al films on the antireflective characteristics of NPAA films consisting of random pore structures is investigated in the wavelength range of 300–1,100 nm at incident light angles (θ_{inc}) of 3°–70°, together with theoretical analysis using a rigorous coupled-wave analysis method. The reflectance strongly depends on the thickness and porosity of NPAA films, resulting from anodization parameters such as applied voltage, anodization time, and pore widening time. For the obtained NPAA film at the initial Al thickness of 100 nm and the applied voltage of 30 V, the surface reflectance is reduced over a wide wavelength region of 300–1,100 nm at normal incidence of ~3°, exhibiting the relatively lower average reflectance (R_{avg}) of ~19 % (i.e., R_{avg} ~ 39 % for the bare Si substrate). The lower angle-dependent reflective properties are observed compared to the bare Si substrate at θ_{inc} = 20°–70° for unpolarized light. The calculated reflectance results of NPAA films show similar trends to the measured data.

1 Introduction

Many semiconductor researchers have used silicon (Si) as a main material for the fabrication of various optical and optoelectronic devices including photovoltaic cells, image sensors, and photo detectors because it is of great technological interest in most of the above applications [1–6]. In these applications, it is very crucial to enhance the light extraction or absorption efficiency of the devices. However, a flat Si surface has high inherent reflectivity of >30 % due to its high refractive index (n_{Si} > 3.4) at visible and near-infrared (NIR) wavelengths, which can degrade the device performance due to the optical losses caused by the Fresnel surface reflection. For high-performance Si-based optoelectronic devices, therefore, efficient antireflection coatings (ARCs) which can suppress the unwanted surface reflection losses are required.

Recently, using an oblique angle deposition (OAD) method, ARCs consisting of nanoporous materials with inclined columnar structured films have been reported [7–9]. The nanoporous films with specified refractive indices can be realized by adjusting the incident vapor flux angle in the OAD process [10, 11]. But this technique needs precise control over the process conditions, which causes some problems in practical applications. As an alternative to the OAD method, a self-assembled nanoporous anodic alumina (NPAA) template, which is prepared by a simple, fast, and cost-effective electrochemical oxidation process of aluminum (Al) films in a particular acidic electrolyte solution, can be employed as an optical thin film. The NPAA template is an aluminum oxide (Al_2O_3) film with self-organized random arrays of uniform parallel nanopores. It has been widely used as a template for fabricating various functional nanostructures [12–15]. The Al_2O_3 film has been also utilized as a passivation layer to suppress the degradation of electrical properties in Si-based optoelectronic devices due to its relatively good mechanical/chemical stability [16–18]. However, NPAA films as an ARC on the Si are rarely reported. In addition, because the NPAA films have no absorption in the visible and NIR wavelength regions, it is very suitable for Si-based optical

B. Dudem · J. W. Leem · M. Choi · J. S. Yu (✉)
Department of Electronics and Radio Engineering, Kyung Hee University, 1732 Deogyeong-daero, Giheung-gu, Yongin-si, Gyeonggi-do 446-701, Republic of Korea
e-mail: jsyu@khu.ac.kr

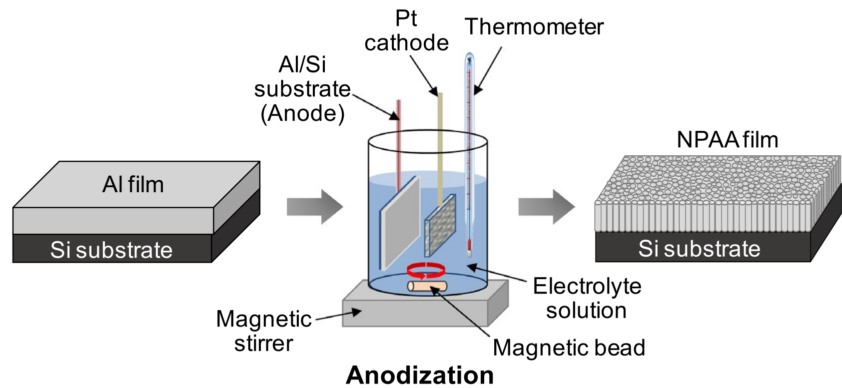

Fig. 1 Schematic of the fabrication process for the NPAA films on Si substrates using the electrochemical anodization of Al films

and optoelectronic devices. The reflection of NPAA films is strongly dependent on their film thickness and porosity (i.e., pore diameter, period, etc.). Furthermore, the hydrophilic property of ARCs can lead to the removal of dust particles and surface contaminants, i.e., self-cleaning [19, 20]. Thus, it is very meaningful to study the surface reflection and wetting behavior of the NPAA films on the Si surface. In this work, we investigated the structural and optical properties of the NPAA films, synthesized by the anodization of Al films, on Si substrates. The angle-dependent reflectance characteristics were also explored. For the fabricated samples, the optical reflection properties were theoretically explored using the rigorous coupled-wave analysis (RCWA) simulation.

2 Experimental and simulation modeling details

Figure 1 shows the schematic of the fabrication process for the NPAA films on Si substrates using the anodization of Al films. The Al films with different film thicknesses of 100, 200, 300, and 500 nm were deposited on the Si substrates with a size of 2.5 × 2.5 cm^2 by using an electron beam evaporation system at room temperature. Before loading, the Si substrates were ultrasonically cleaned in acetone, methanol, and deionized (DI) water. Then, the samples were dried in flowing nitrogen (N_2) gas. Prior to the anodization, the side edges of squared samples were covered by the polydimethylsiloxane (Sylgard 184, Dow Corning Co.) and subsequently dried at 75 °C for 1 h. This is useful to avoid the uneven distribution of electric field at the edges of samples and to prevent the pilling of Al at the interface between the Al and Si substrate [21]. To obtain the optimized NPAA films with efficient antireflection, the anodization of Al films on Si substrates was performed under a constant stirring speed of 200 rpm in 5 wt% phosphoric acid solution at room temperature by varying the process parameters such as anodization time, applied voltage, and pore widening time. These process parameters affect the porosity, which is related to the pore diameter, period, and barrier layer thickness of NPAA films, within the anodized Al films, which results in the change of reflectance properties. After the anodization process, the samples were rinsed with acetone, methanol, and DI water and subsequently were dried with N_2 gas. The additional pore widening was carried out by dipping the anodized samples into 5 wt% phosphoric acid solution at 30 °C.

Field-emission scanning electron microscope (FE-SEM; LEO SUPRA 55, Carl Zeiss) and atomic force microscope (AFM; D3100, Veeco) measurements were carried out to investigate surface morphologies and cross-sectional features of the fabricated samples. The reflectance property of samples was evaluated by using a UV–Vis–NIR spectrophotometer (Cary 5000, Varian) with an integrating sphere at near-normal incidence of ~3°. Spectroscopic ellipsometry (V-VASE, J. A. Woollam Co. Inc.) was used to measure the angle-dependent reflectance at incident angles of 20°–70° for unpolarized light. The contact angles of water droplets on the surfaces of samples were taken by using a contact angle measurement system (Phoenix-300, SEO Co., Ltd.). The measured contact angle values at different positions were averaged as a single value. For theoretical optical analysis of the samples, the RCWA calculations were performed using a commercial software (*DiffractMOD* 3.1, Rsoft Design Group). To design the theoretical models, the NPAA films with pore structures on Si substrates were roughly represented by cylindrical pore pattern arrays with a periodic four-fold rectangular symmetry, for simplicity. For the modeling of the NPAA films, further details can be referred in our previous works [22, 23]. We assumed that the incident light enters from air to the structure at incident angles of 0°–70°, and the thickness of Si substrate is set to 500 µm. The refractive indices of Si and Al_2O_3 used in this calculation were referred from *SOPRA N&K Database* [24].

3 Results and discussion

Figure 2 shows (a) the top-view and cross-sectional SEM images and (b) the measured reflectance spectra of the

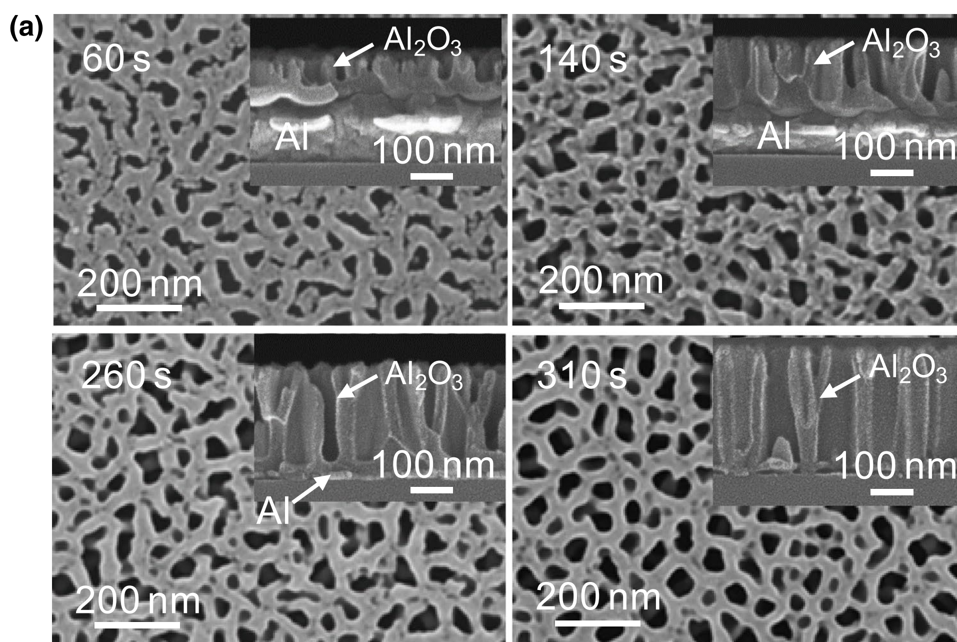

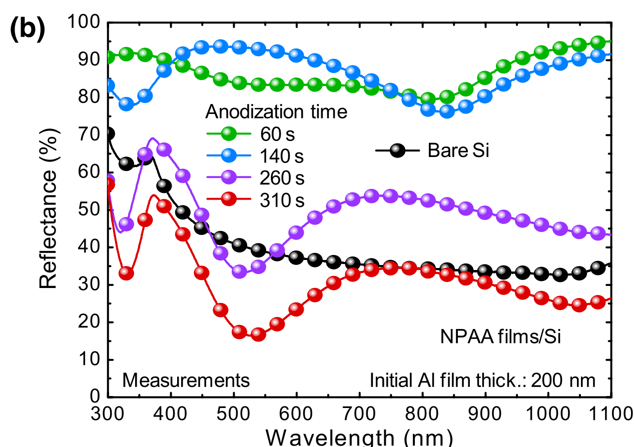

Fig. 2 **a** Top-view and cross-sectional SEM images and **b** measured reflectance spectra of the NPAA films on Si substrates for the initial Al film thickness of 200 nm at 30 V

NPAA films on Si substrates for the initial Al film thickness of 200 nm at an applied voltage of 30 V. As the anodization time increased, the nucleated pores started to grow up and the NPAA layer thickness increased, as shown in Fig. 2a. If the anodization time is short, a little amount of Al gets anodized (or is consumed) to form an NPAA film. As the anodization time increased to 60, 140, and 260 s, most of the Al was consumed to produce the NPAA film, indicating the thicknesses of ~115, 180, and 260 nm, respectively. The pore area with an average distance of ~100 nm between adjacent pores in the NPAA film was also observed in the SEM images of Fig. 2a. The NPAA films were formed by the anodization of Al at certain electrolyte conditions, and most of the researches mentioned the formation of NPAA follows the preferential growth mechanism [25]. During the anodization initially within few seconds, a thin and dense alumina layer was formed on the Al surface. As the anodization time further increased, small pits started to be formed on alumina surface. These pits are used as nuclei to form the pores on alumina surface and further grow throughout the aluminum. On the contrary, at the anodization time of 310 s, the 200-nm-thick Al layer was nearly consumed and changed into the NPAA film, exhibiting a thickness of ~285 nm and an average pore diameter of ~55 nm. For the anodized NPAA films, the increase of film thickness was observed due to the volume expansion factor difference between aluminum and alumina [26]. Due to the pore generation in alumina, the volume expansion differences may occur. The volume expansion factor of porous alumina films as well as the pore cell dimensions strongly depends on the electric field strength [27, 28]. When the electric field is applied to anodize the Al, the greater electric field strength (or current density) is located across the oxide/Al interface, whereas its lower amount was induced across the electrolyte solution/oxide interface, compared to the average applied electric field strength across the anode.

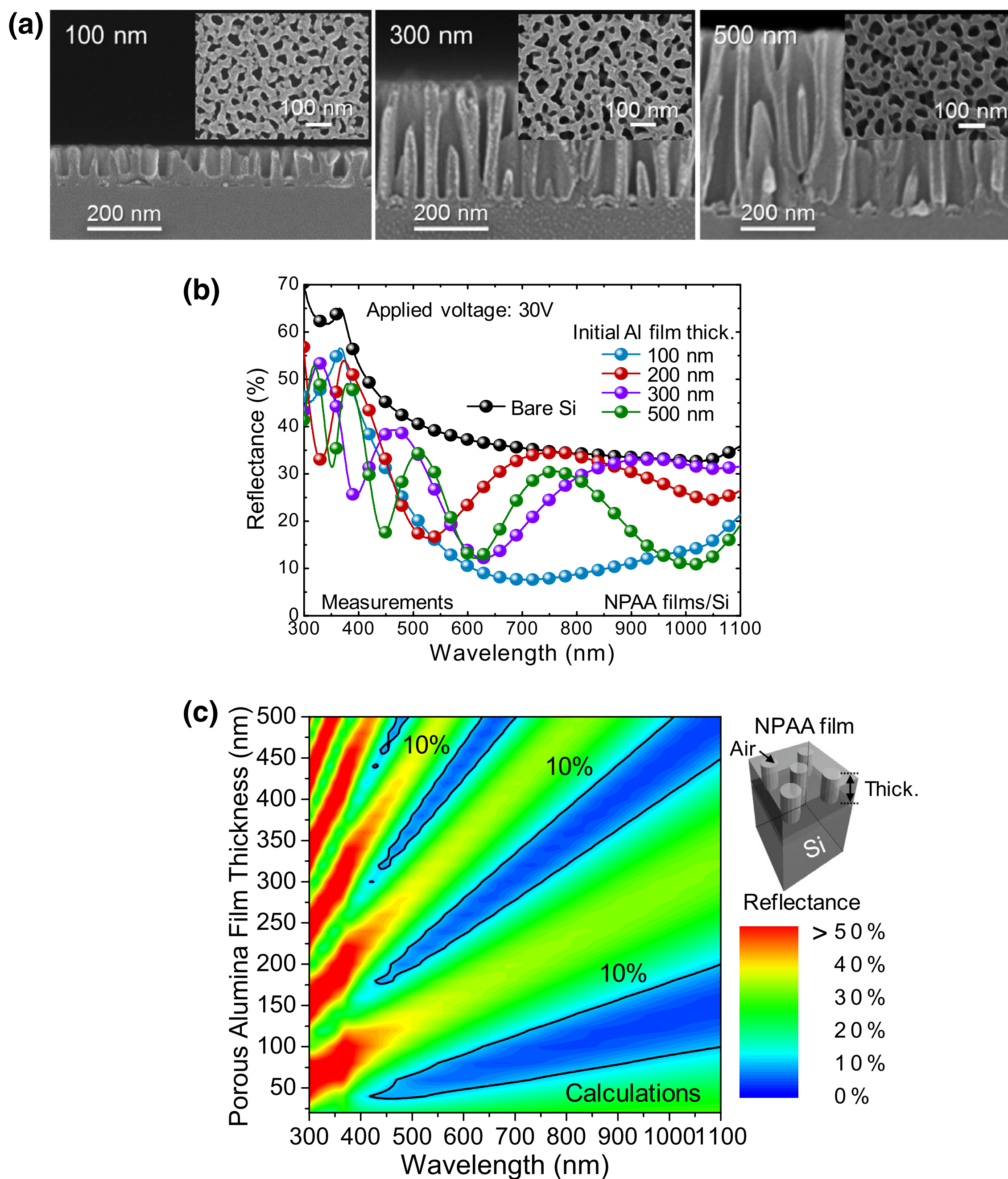

Fig. 3 **a** Top-view and cross-sectional SEM images of the NPAA films on Si substrates with different initial Al thicknesses of 100, 300, and 500 nm at 30 V, **b** measured reflectance spectra of the corresponding samples, and **c** contour plots of variation of the calculated reflectance spectra as functions of thickness of NPAA film and wavelength. The 3D scale-modified simulation model with a periodic fourfold rectangular symmetry pore array used in these calculations is also shown in (**c**)

The lower current density leads to the formation of pores by the dissolution of Al ions, while, at the higher current density, the alumina film is formed through the Al/oxide interface. Thus, the formation of pores may be enhanced by the increase in the formation efficiency of alumina films, which causes the volume expansion of alumina. For comparison, the reflectance spectrum of bare Si substrate is also shown in Fig. 2b. In the reflection properties of Fig. 2b, for the non-completely anodized samples with anodization times of 60, 140, and 260 s, the reflectance spectra were higher than that of the bare Si substrate due to the remained Al films, as can be seen in Fig. 2a. On the other hand, the NPAA films with the anodization time of 310 s showed a lower reflectivity compared with the bare Si substrate over

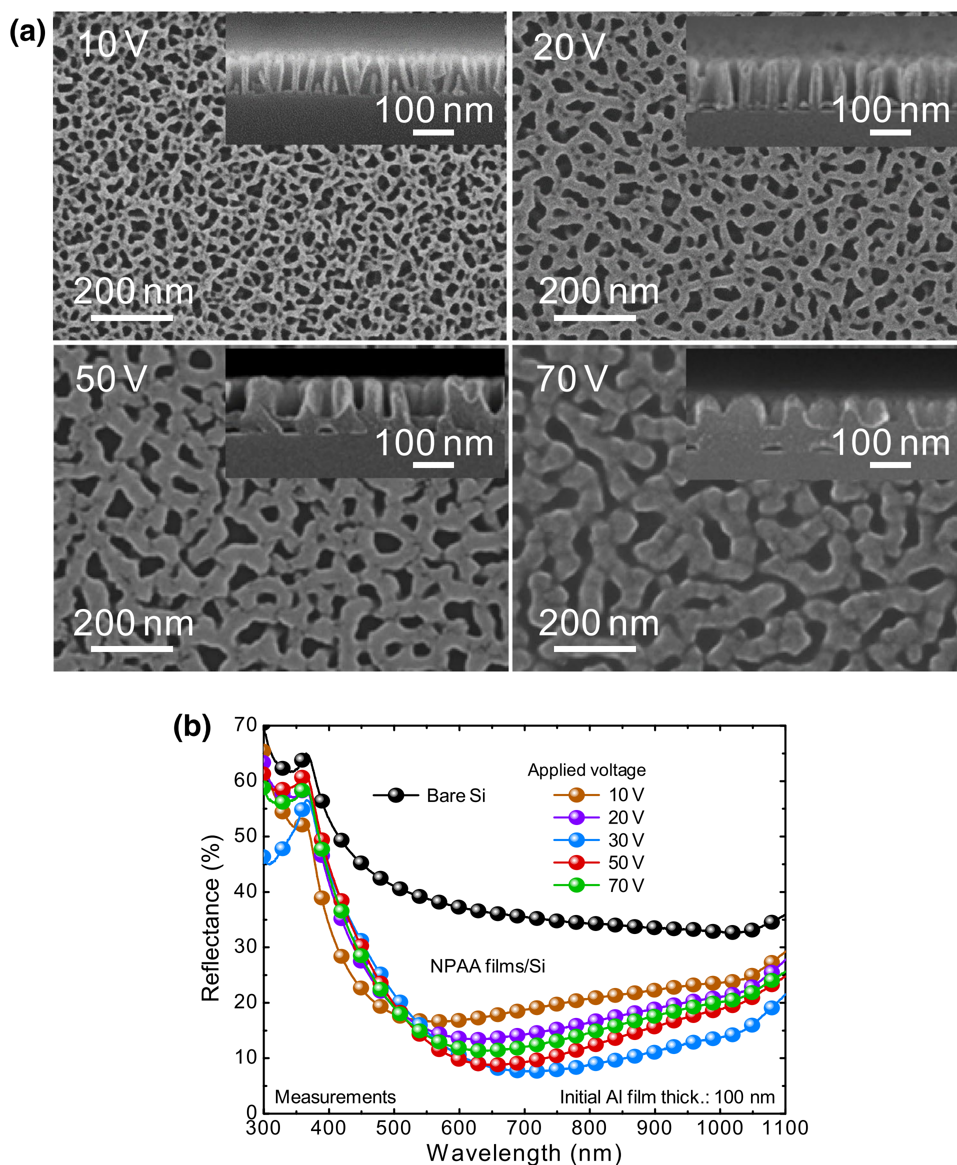

Fig. 4 **a** Top-view and cross-sectional SEM images and **b** measured reflectance spectra of the NPAA films on Si substrates at different applied voltages of 10, 20, 30, 50, and 70 V for the 100-nm-thick initial Al film

a wide wavelength range of 300–1,100 nm, indicating an average reflectance (R_{avg}) value of ~23 % (i.e., R_{avg} ~ 39 % for the bare Si substrate). This is attributed to the nanoporous structured alumina film with a lower refractive index than that of Si, which creates a gradient effective refractive index profile between air and the Si via the NPAA film.

Figure 3a shows the top-view and cross-sectional SEM images of the NPAA films on Si substrates with different initial Al thicknesses of 100, 300, and 500 nm at 30 V. As shown in Fig. 3a, all the Al films with different thicknesses of 100, 300, and 500 nm were completely converted to the NPAA films with thicknesses of ~140 ± 5, 370 ± 9, and 570 ± 15 nm and average pore diameter sizes of ~55 ± 5 nm, respectively. It can be also observed that the barrier alumina layer with a thickness of about 25 ± 10 nm remained. The measured reflectance spectra of the corresponding samples and the contour plots of variation of the calculated reflectance spectra as functions of thickness of NPAA film and wavelength are shown in Fig. 3b, c, respectively. The reflectance spectra depend on the thickness of NPAA films. By increasing the thickness of initial Al films from 100 to 500 nm, the maxima and the number of interference oscillations in the reflectance spectrum were decreased and increased, respectively. The R_{avg} value of NPAA films was increased from ~19 % for the 100-nm-thick initial Al film to ~26 % for the 500 nm film, exhibiting the minimum R value of ~7.6 % at wavelengths of 695–725 nm for the NPAA film at the 100-nm-thick initial Al film. To study the influence of the thickness on the reflectance of NPAA film, the RCWA simulation was performed. The three-dimensional (3D) scale-modified simulation model with a periodic fourfold rectangular symmetry pore

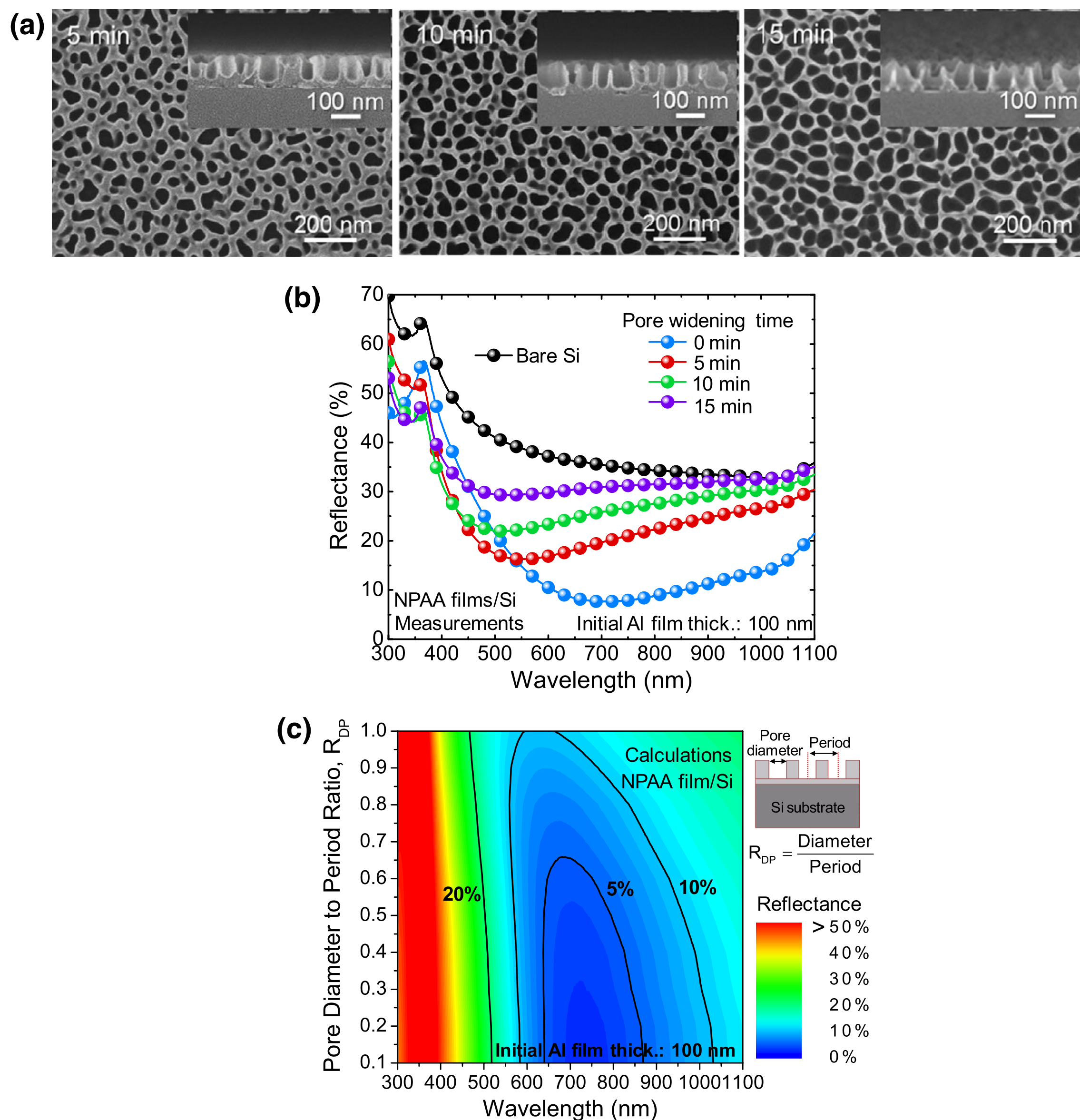

Fig. 5 **a** Top-view and cross-sectional SEM images, **b** measured reflectance spectra of the NPAA films with 100-nm-thick initial Al films on Si substrates for different additional pore widening times of 0, 5, 10, and 15 min at 30 V, and **c** contour plot of variations of the calculated reflectance spectra of NPAA film as functions of pore diameter to period ratio (R_{DP}) and wavelength

array used in these calculations is also shown in Fig. 3c. We assumed that the pore diameter, period, and barrier alumina layer thickness of NPAA film were set to be 50, 100, and 25 nm, respectively. As shown in Fig. 3c, as the thickness of NPAA film is increased, the number of interference oscillations in the reflectance spectrum is also increased. Although there are discrepancies at some wavelengths between the measured and calculated results owing to the geometrical difference in the simulation model and the fabricated structure as well as the refractive index mismatch of the materials used in this experiment and calculation, they roughly give a similar tendency in a wide range of wavelengths.

Figure 4 shows (a) the top-view and cross-sectional SEM images and (b) the measured reflectance spectra of the NPAA films on Si substrates at different applied voltages of 10, 20, 30, 50, and 70 V for the 100-nm-thick initial Al film. As the applied voltage was increased, the current density was also increased along the oxide/Al and electrolyte/oxide interfaces. This means that the electric field strength is enhanced across the electrodes. The progressive increment of the electric field (or current density) results in the higher growth and dissolution rate of oxide across the oxide/Al and electrolyte/oxide interface, respectively [29]. Similarly, the pore diameter, period, and barrier layer

thickness also were varied by the intensity of applied voltage [29, 30]. As can be seen in the SEM images of Fig. 4a, the pore diameter, pore separation, and the pore wall thickness become larger by increasing the applied voltage. Moreover, the thickness of barrier layer of dense alumina without any pores was increased when the applied voltage became higher. This indicates that the growth of alumina is more dominant than the dissolution of alumina at higher applied voltages. Thus, the change of barrier layer thickness as a function of applied voltage influences the optical properties of NPAA films due to the difference of refractive indices between the dense and porous alumina layers. The average pore diameters and periods of NPAA films were varied from ~35 and 48 nm at 10 V to ~72 and 105 nm at 70 V, exhibiting the change of thickness in barrier alumina layers from ~16 nm at 10 V to ~48 nm at 70 V. From the reflectance spectra in Fig. 4b, it can be confirmed that the R_{avg} value was reduced from 25 % at 10 V to 19 % at 30 V and increased to 22 % at 70 V. This is ascribed to the variation of porosity of NPAA films as well as the barrier alumina dense layer, as mentioned above.

The effect of porosity by varying the additional pore widening process on the structural and optical properties of NPAA films was also studied. Figure 5 shows the (a) top-view and cross-sectional SEM images, (b) measured reflectance spectra of the NPAA films with 100-nm-thick initial Al films on Si substrates for different additional pore widening times of 0, 5, 10, and 15 min at applied voltage of 30 V, and (c) contour plot of variations of the calculated reflectance spectra of NPAA film as functions of pore diameter to period ratio (R_{DP}) and wavelength. The size of pore diameter can be controlled by adjusting the dipping duration in acidic solution. For the NPAA film with an average pore diameter of ~55 nm, an additional pore widening process was performed by varying the pore widening time to 5, 10, and 15 min. The average pore diameter was gradually increased from ~65.5 nm at 5 min to ~81.5 nm at 15 min. From the cross-sectional SEM images of the samples, it is clear that the dissolution rate of alumina at the surface of pores is faster when compared to the deeper side of pores. As the pore widening time was increased, the pore diameter increased while simultaneously both the thicknesses of pore wall and barrier layer were decreased. Therefore, at the longer pore widening time of 15 min, the pore size became greater and the barrier alumina layer was completely dissolved, and thus, the Si surface was exposed at the bottom of pores. As shown in Fig. 5b, the reflectance was gradually increased and low reflectance region shifted toward the short wavelength range by increasing the pore widening time from 5 to 15 min, exhibiting the increase of R_{avg} value from 19 % at 0 min to 35 % at 15 min. This is due to the decrease of effective refractive index of NPAA film due to the

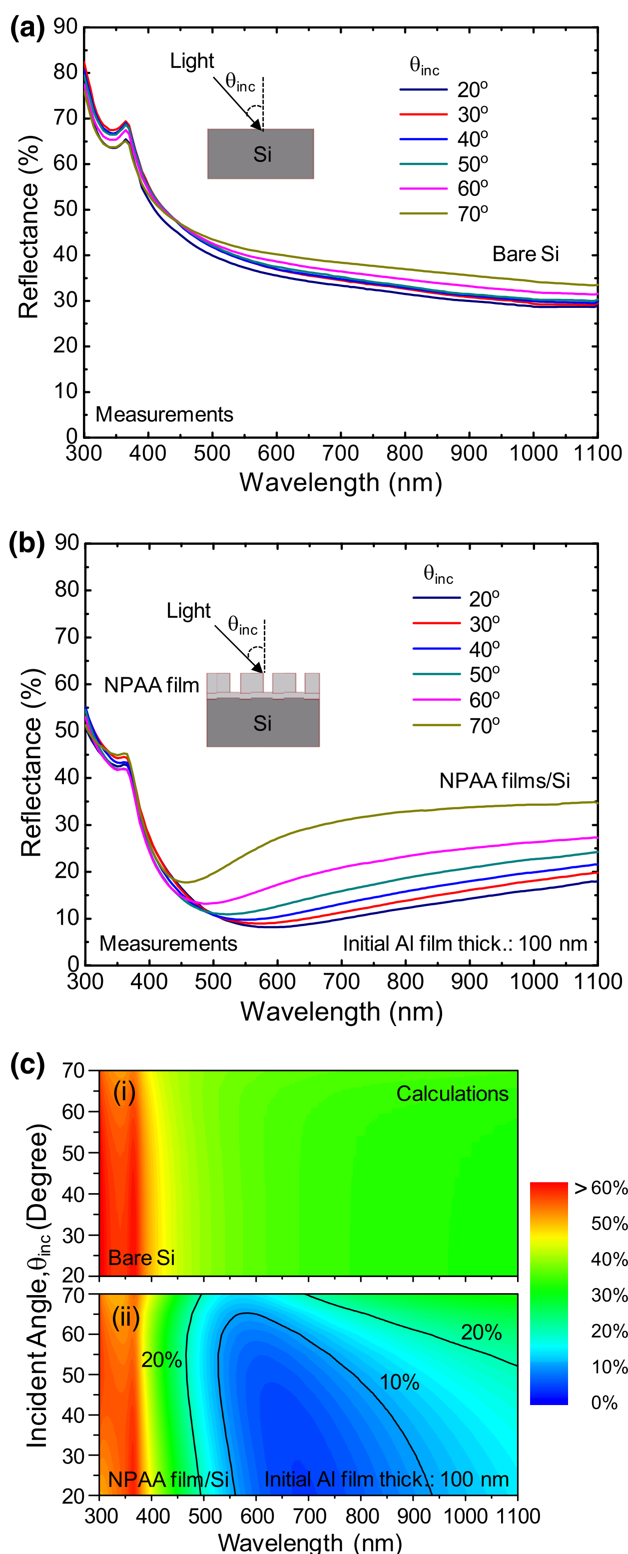

Fig. 6 Measured reflection spectra of the **a** bare Si substrate and **b** NPAA film/Si substrate at 30 V for the 100-nm-thick initial Al film without additional pore widening process and **c** contour plots of variation of the calculated reflectance spectra of the corresponding structures at different incident angles (θ_{inc}) of 20°–70° for unpolarized light

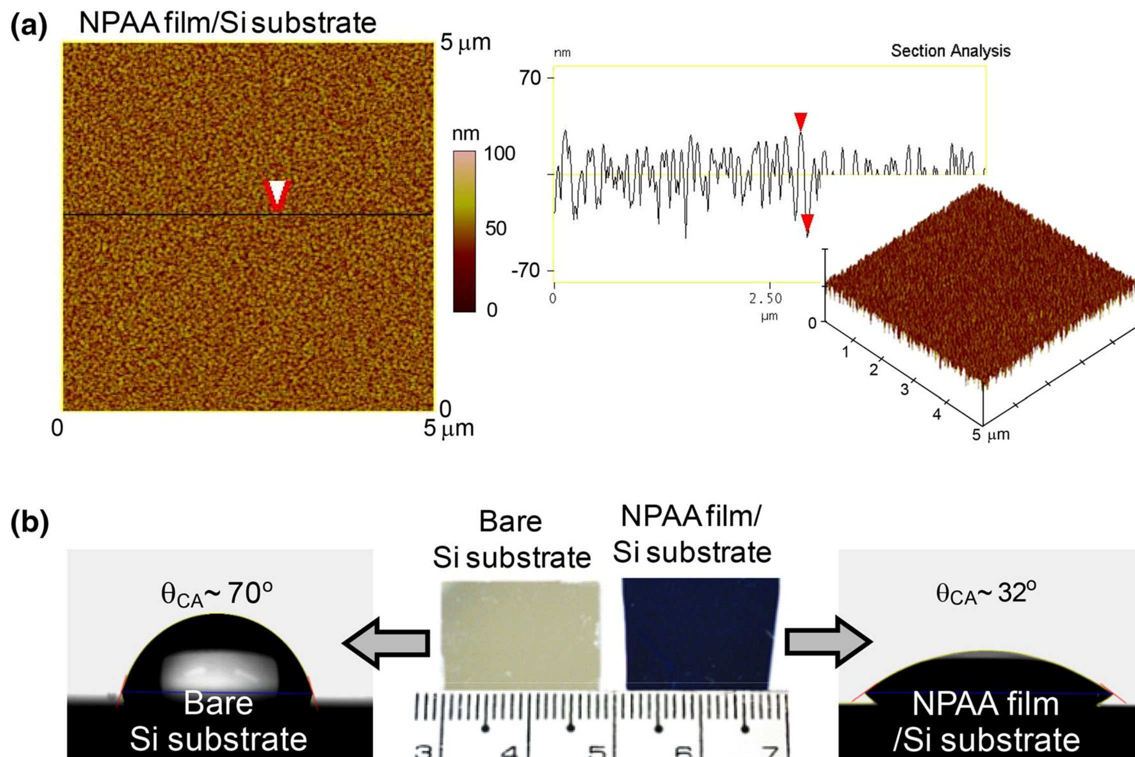

Fig. 7 **a** 5 × 5 μm^2 AFM scan images of the NPAA film on the Si substrate at 30 V for the 100-nm-thick initial Al film without any pore widening treatment and **b** photographic images of the bare Si substrate and fabricated NPAA film/Si substrate and the water droplets on the surface of the corresponding samples

increase of porosity within the alumina layer with pore structures caused by the collapsed pores at side walls and reduced barrier alumina layer. For solar cell applications, it is necessary to investigate the solar-weighted reflectance (R_{SWR}) which is defined by the ratio of the usable photons reflected to the total useable photons. The R_{SWR} can be estimated by normalizing the reflectance and the terrestrial AM1.5G spectra integrated over a wavelength range of 300–1,100 nm [31, 32]. For the NPAA film without an additional pore widening process, the lower R_{SWR} value of ~16 % was obtained compared with the bare Si substrate (i.e., R_{SWR} ~ 38 %). The influence of porosity of NPAA films was investigated on their reflectance by varying the R_{DP}. In the RCWA calculations of Fig. 5c, similarly, the reflectance spectra of NPAA films on the Si substrate were slightly increased and low reflectance band shifted toward the short wavelength region, indicating a similar trend with the measured data in Fig. 5b.

Figure 6 shows the measured reflectance spectra of the (a) bare Si substrate and (b) NPAA film/Si substrate at 30 V for the 100-nm-thick initial Al film without additional pore widening process, and (c) the contour plots of variation of the calculated reflectance spectra of the corresponding structures at different incident angles (θ_{inc}) of 20°–70° for unpolarized light. As shown in Fig. 6a, for the bare Si substrate, all the reflectance spectra were higher than ~30 % at θ_{inc} = 20°–70°. On the other hand, the NPAA film significantly reduced the reflectance in wide ranges of wavelength and incident angles compared with the bare Si substrate. Its R_{avg} value is slightly increased from ~16 % at $\theta_{inc} = 20°$ to ~31 % at $\theta_{inc} = 70°$, exhibiting the R_{avg} value of ~22 % over in the θ_{inc} range of 20°–70° (i.e., R_{avg} ~ 40 % for the bare Si substrate). At wavelengths of 300–1,100 nm and incident angles of 20°–70°, the NPAA film/Si substrate exhibited a much lower average R_{SWR} value of ~18 % than that (i.e., average R_{SWR} ~ 38 %) of the bare Si substrate. In Fig. 6c, the theoretically calculated reflectance spectra also agree well with the measured data in Fig. 6a, b.

Figure 7 shows (a) the 5 × 5 μm^2 AFM scan images of the NPAA film on the Si substrate at 30 V for the 100-nm-thick initial Al film without any pore widening treatment and (b) the photographic images of the bare Si substrate and fabricated NPAA film/Si substrate and the water droplets on the surface of the corresponding samples. From the AFM images in Fig. 7a, the pores with a random array were well formed in the alumina film, exhibiting the average distance of ~100 ± 10 nm between the adjacent pores and the average pore height of ~110 ± 20 nm. As can be seen in Fig. 7b, the surface of the NPAA film/Si substrate

clearly appeared to be dark blue because of its low reflectance property in the visible wavelength range in comparison with the bare Si substrate. To investigate the surface macroscopic property on the wetting behavior of the NPAA film with the lowest reflectivity, the water contact angle was estimated. Both the samples exhibited a hydrophilic surface. However, the surface of the NPAA film revealed a lower water contact angle (θ_{CA}) of ~32° than that (i.e., θ_{CA} ~ 70°) of the bare Si substrate. Therefore, the hydrophilic surface of NPAA films with lower θ_{CA} values, which can spread the liquid on nanoporous structures, can be used for the potential applications in printing, coating, and self-cleaning [19, 33].

4 Conclusion

The NPAA films with random pore structures were successfully fabricated on Si substrates by the electrochemical anodization of Al. The influence of the porosity and thickness of NPAA films/Si substrates was experimentally and theoretically investigated on the structural and optical reflectance properties as well as the surface wetting behavior by varying anodization parameters such as anodization time, initial Al thickness, applied voltage, and pore widening time. The optimized NPAA film/Si substrate was obtained for the anodizing condition at 30 V for 100-nm-thick initial Al film. The sample exhibited a hydrophilic surface with θ_{CA} value of ~32° and R_{avg} value of ~19 % at wavelengths 300–1,100 nm. These values are much lower than those (θ_{CA} ~ 70° and R_{avg} of ~39 %) of the bare Si substrate. For angle-dependent reflectance characteristics, it also showed the lower reflectance spectra at θ_{inc} values of 20°–70°. The calculated reflectance results by RCWA simulations reasonably indicate a similar behavior with the measured data. Thus, these results can give a promising potential of NPAA films with relatively good mechanical/chemical and long-term stabilities for broadband and omnidirectional antireflection properties as well as the self-cleaning function in Si-based optoelectronic device applications.

Acknowledgments This work was supported by the National Research Foundation of Korea (NRF) Grant funded by the Korea government (MSIP) (No. 2013-068407).

References

1. D.E. Carlson, C.R. Wronski, Appl. Phys. Lett. **28**, 671 (1976)
2. B. Yan, G. Yue, L. Sivec, J. Yang, S. Guha, C.S. Jiang, Appl. Phys. Lett. **99**, 113512 (2011)
3. W.S. Wong, S. Raychaudhuri, R. Lujan, S. Sambandan, R.A. Street, Nano Lett. **11**, 2214 (2011)
4. K. Seo, M. Wober, P. Steinvurzel, E. Schonbrun, Y. Dan, T. Ellenbogen, K.B. Crozier, Nano Lett. **11**, 1851 (2011)
5. I. Goykhman, B. Desiatov, J. Khurgin, J. Shappir, U. Levy, Opt. Express **20**, 28594 (2012)
6. J. Konle, H. Presting, H. Kibbel, K. Thonke, R. Sauer, Solid State Electron. **45**, 1921 (2001)
7. J.-Q. Xi, M.F. Schubert, J.K. Kim, E.F. Schubert, M. Chen, S.-Y. Lin, W. Liu, J.A. Smart, Nat. Photon. **1**, 176 (2007)
8. J.W. Leem, J.S. Yu, Opt. Express **19**, A258 (2011)
9. S. Sarkar, S.K. Pradhan, Appl. Surf. Sci. **290**, 509 (2014)
10. J.W. Leem, J.S. Yu, Thin Solid Films **518**, 6285 (2010)
11. J.W. Leem, J.S. Yu, Nanoscale **5**, 2520 (2013)
12. T. Yang, X. Wang, W. Liu, Y. Shi, F. Yang, Opt. Express **21**, 18207 (2013)
13. J.D. Berrigan, T. McLachlan, J.R. Deneault, Y. Cai, T.-S. Kang, M.F. Durstock, K.H. Sandhage, J. Mater. Chem. A **1**, 128 (2013)
14. M. Aramesh, K. Fox, D.W.M. Lau, J. Fang, K. Ostrikov, S. Prawer, J. Cervenka, Carbon **75**, 452 (2014)
15. J. Zuidema, X. Ruan, T.S. Fisher, Opt. Express **21**, 22053 (2013)
16. S. Miyajima, J. Irikawa, A. Yamada, M. Konagai, Appl. Phys. Express **3**, 012301 (2010)
17. R. Hezel, K. Jaeger, J. Electrochem. Soc. **136**, 518 (1989)
18. T. Kumeria, A. Santos, D. Losic, Sensors **14**, 11878 (2014)
19. J.W. Leem, J.S. Yu, J. Heo, W.K. Park, J.H. Park, W.J. Cho, D.E. Kim, Sol. Energy Mater. Sol. Cells **120**, 555 (2014)
20. K. Guan, Surf. Coat. Technol. **191**, 155 (2005)
21. R. Nayak, D.R. Knapp, Anal. Chem. **79**, 4950 (2007)
22. J.W. Leem, Y.P. Kim, J.S. Yu, J. Opt. Soc. Am. B **29**, 357 (2012)
23. J.W. Leem, K.S. Chung, J.S. Yu, Curr. Appl. Phys. **12**, 291 (2012)
24. SOPRA, N&K Database (2014). http://refractiveindex.info. Accessed 1 May 2014
25. G.E. Thompson, R.C. Furneaux, G.C. Wood, J.A. Richardson, J.S. Goode, Nature **272**, 433 (1978)
26. F. Zhou, A.K.M. Al-Zenati, A. Baron-Wiecheć, M. Curioni, S.J. Garcia-Vergara, H. Habazaki, P. Skeldon, G.E. Thompson, J. Electrochem. Soc. **158**, C202 (2011)
27. I. Vrublevsky, V. Parkoun, J. Schreckenbach, G. Marx, Appl. Surf. Sci. **220**, 51 (2003)
28. I. Vrublevsky, V. Parkoun, V. Sokol, J. Schreckenbach, G. Marx, Appl. Surf. Sci. **222**, 215 (2004)
29. J.P. O'Sullivan, G.C. Wood, Proc. R. Soc. Lond. Ser. A **317**, 511 (1970)
30. G. Paolini, M. Masoero, F. Sacchi, M. Paganelli, J. Electrochem. Soc. **112**, 32 (1965)
31. J.W. Leem, Y.M. Song, J.S. Yu, Nanoscale **5**, 10455 (2013)
32. H.V. Han, C.C. Lin, Y.L. Tsai, H.C. Chen, K.J. Chen, Y.L. Yeh, W.Y. Lin, H.C. Kuo, P. Yu, Sci. Rep. **4**, 5734 (2014)
33. Z. Li, J. Wang, Y. Zhang, J. Wang, L. Jiang, Y. Song, Appl. Phys. Lett. **97**, 233107 (2010)